

University of Groningen

**Local deformation gradients in epitaxial Pb(Zr<sub>0.2</sub>Ti<sub>0.8</sub>)O<sub>3</sub> layers investigated by transmission electron microscopy**

Denneulin, T.; Wollschlaeger, N.; Everhardt, A. S.; Farokhipoor, S.; Noheda, B.; Snoeck, E.; Hytch, M.

*Published in:*  
Journal of Physics-Condensed Matter

*DOI:*  
[10.1088/1361-648X/aabd00](https://doi.org/10.1088/1361-648X/aabd00)

**IMPORTANT NOTE: You are advised to consult the publisher's version (publisher's PDF) if you wish to cite from it. Please check the document version below.**

*Document Version*  
Publisher's PDF, also known as Version of record

*Publication date:*  
2018

[Link to publication in University of Groningen/UMCG research database](#)

*Citation for published version (APA):*

Denneulin, T., Wollschlaeger, N., Everhardt, A. S., Farokhipoor, S., Noheda, B., Snoeck, E., & Hytch, M. (2018). Local deformation gradients in epitaxial Pb(Zr<sub>0.2</sub>Ti<sub>0.8</sub>)O<sub>3</sub> layers investigated by transmission electron microscopy. *Journal of Physics-Condensed Matter*, 30(21), Article 215701. <https://doi.org/10.1088/1361-648X/aabd00>

**Copyright**

Other than for strictly personal use, it is not permitted to download or to forward/distribute the text or part of it without the consent of the author(s) and/or copyright holder(s), unless the work is under an open content license (like Creative Commons).

The publication may also be distributed here under the terms of Article 25fa of the Dutch Copyright Act, indicated by the "Taverne" license. More information can be found on the University of Groningen website: <https://www.rug.nl/library/open-access/self-archiving-pure/taverne-amendment>.

**Take-down policy**

If you believe that this document breaches copyright please contact us providing details, and we will remove access to the work immediately and investigate your claim.

*Downloaded from the University of Groningen/UMCG research database (Pure): <http://www.rug.nl/research/portal>. For technical reasons the number of authors shown on this cover page is limited to 10 maximum.*

PAPER

# Local deformation gradients in epitaxial $\text{Pb}(\text{Zr}_{0.2}\text{Ti}_{0.8})\text{O}_3$ layers investigated by transmission electron microscopy

To cite this article: T Denneulin *et al* 2018 *J. Phys.: Condens. Matter* **30** 215701

View the [article online](#) for updates and enhancements.

## Related content

- [Configuration and local elastic interaction of ferroelectric domains and misfit dislocation in  \$\text{PbTiO}\_3/\text{SrTiO}\_3\$  epitaxial thin films](#)  
Takanori Kiguchi, Kenta Aoyagi, Yoshitaka Ehara *et al.*
- [Polydomain structures in ferroelectric and ferroelastic epitaxial films](#)  
Alexander L Roytburd, Jun Ouyang and Andrei Artemev
- [Dark-field electron holography for the mapping of strain in nanostructures: correcting artefacts and aberrations](#)  
M J Hÿtch, F Houdellier, F Hÿe *et al.*

# Local deformation gradients in epitaxial $\text{Pb}(\text{Zr}_{0.2}\text{Ti}_{0.8})\text{O}_3$ layers investigated by transmission electron microscopy

T Denneulin<sup>1,2</sup>, N Wollschläger<sup>3</sup>, A S Everhardt<sup>4</sup>, S Farokhipoor<sup>4</sup>, B Noheda<sup>4</sup>, E Snoeck<sup>1</sup> and M Hÿtch<sup>1</sup>

<sup>1</sup> CEMES, CNRS, 29 rue Jeanne Marvig, 31055 Toulouse, France

<sup>2</sup> Ernst Ruska Centre for Microscopy and Spectroscopy with Electrons and Peter Grünberg Institute, Forschungszentrum Jülich, Jülich 52425, Germany

<sup>3</sup> BAM, Unter den Eichen 87, 12205 Berlin, Germany

<sup>4</sup> Zernike Institute for Advanced Materials, University of Groningen, 9747 AG Groningen, Netherlands

E-mail: [t.denneulin@fz-juelich.de](mailto:t.denneulin@fz-juelich.de)

Received 18 February 2018, revised 29 March 2018

Accepted for publication 10 April 2018

Published 30 April 2018



## Abstract

Lead zirconate titanate samples are used for their piezoelectric and ferroelectric properties in various types of micro-devices. Epitaxial layers of tetragonal perovskites have a tendency to relax by forming  $90^\circ$  ferroelastic domains. The accommodation of the  $a/c/a/c$  polydomain structure on a flat substrate leads to nanoscale deformation gradients which locally influence the polarization by flexoelectric effect. Here, we investigated the deformation fields in epitaxial layers of  $\text{Pb}(\text{Zr}_{0.2}\text{Ti}_{0.8})\text{O}_3$  grown on  $\text{SrTiO}_3$  substrates using transmission electron microscopy (TEM). We found that the deformation gradients depend on the domain walls inclination ( $+45^\circ$  or  $-45^\circ$  to the substrate interface) of the successive  $90^\circ$  domains and we describe three different  $a/c/a$  domain configurations: one configuration with *parallel*  $a$ -domains and two configurations with perpendicular  $a$ -domains (*V-shaped* and *hat- $\wedge$ -shaped*). In the *parallel* configuration, the  $c$ -domains contain horizontal and vertical gradients of out-of-plane deformation. In the *V-shaped* and *hat- $\wedge$ -shaped* configurations, the  $c$ -domains exhibit a bending deformation field with vertical gradients of in-plane deformation. Each of these configurations is expected to have a different influence on the polarization and so the local properties of the film. The deformation gradients were measured using dark-field electron holography, a TEM technique, which offers a good sensitivity (0.1%) and a large field-of-view (hundreds of nanometers). The measurements are compared with finite element simulations.

Keywords: ferroelectric, PZT, strain, electron holography, TEM

(Some figures may appear in colour only in the online journal)

## 1. Introduction

Ferroelectric and piezoelectric thin films have found a large number of applications in memories [1] and micro-electro-mechanical systems (MEMS) [2]. Above a certain critical thickness, tetragonal perovskite materials have a tendency to form  $90^\circ$  ferroelectric/ferroelastic domains to relieve the interfacial stress with the substrate [3–6]. The resulting

domain patterns can be exploited to control the dielectric [7] or piezoelectric response [8], and create memories with high information density [9]. The accommodation of such a twinned structure on a flat substrate leads to local strain gradients, in a commonly used  $\text{PbTiO}_3$  perovskite material [10]. These strain gradients are huge because of the small length-scale and they can have a strong impact on the properties of the film. Nanoscale strain gradients can, for instance, influence

the polarization by the flexoelectric effect [10, 11], lead to asymmetric hysteresis loops [12] and change the mobility of the domain walls [13]. Therefore, a precise description of the local domain configurations with their respective strain fields is important to understand the ferroelectric and piezoelectric behavior of the film.

Here, we have investigated the strain fields in tetragonal  $\text{Pb}(\text{Zr}_{0.2}\text{Ti}_{0.8})\text{O}_3$  (PZT) thin films grown epitaxially on cubic  $\text{SrTiO}_3$  (STO) substrates. Cross-sectional TEM (transmission electron microscopy) images have shown that such PZT layers contain large  $c$ -domains (the  $c$ -axis, which is also the polarization axis, being out-of-plane) and smaller needle-shaped  $a$ -domains (the  $a$ -axis being out-of-plane and, thus, the polarization in-plane) [14–16]. Figure 1 shows a bright-field TEM image of a 100 nm thick PZT layer grown on STO. The  $a/c$  domain walls lie along the  $\{101\}$  lattice planes and they have two possible inclinations with respect to the substrate interface:  $+45^\circ$  or  $-45^\circ$ . Therefore, three different  $a/c/a$  domain configurations can be distinguished depending on the inclination of the neighboring  $a$ -domains: a *parallel-//*-shaped configuration with two parallel  $a$ -domains separated by a parallelogram-shaped  $c$ -domain (in the middle of figure 1); a *V-shaped* configuration with two  $a$ -domains joining at the interface with the substrate (left-hand side of figure 1) and a *hat-^*-shaped configuration with two  $a$ -domains joining near the surface (right-hand side of figure 1).

This paper will discuss these three configurations and the deformation fields that they produce using two TEM techniques: geometrical phase analysis (GPA) [17] applied to aberration-corrected high resolution TEM (HRTEM) images and dark-field electron holography (DFEH) [18]. In GPA, the atomic fringes of a HRTEM image are treated as spatial frequencies. The phase of a given set of lattice planes is reconstructed by calculating the Fourier transform (FT) of the HRTEM image, selecting the corresponding reflection in Fourier space and performing an operation on the complex image obtained after inverse Fourier transform ( $\text{FT}^{-1}$ ). The lattice deformation is then obtained from the gradient of the phase image calculated in the direction of the corresponding reciprocal lattice vector  $\mathbf{g}$ . The spatial resolution is limited by the size of the mask used to select the lattice reflection. Here, the spatial resolution is 2 nm and the deformation sensitivity is  $\pm 0.5\%$ . In DFEH, an electron beam diffracted by a given set of lattice planes is first selected using an objective aperture. Second, the part of the beam diffracted by the substrate and the part of the beam diffracted by the thin film are superimposed thanks to an electron biprism placed below the specimen. This produces an interference pattern (the hologram), from which a phase image and a deformation map can be reconstructed (details of the method are given in [18]). The hologram can be seen as a moiré pattern of the crystal lattice and the use of large holographic fringes (2 nm large in the present study) provides a better strain sensitivity than the analysis of atomic fringes in HRTEM images [19, 20]. For the conditions used in this paper, the strain sensitivity is  $\pm 0.1\%$  and the spatial resolution is 6 nm. This technique will be used to evidence the deformation gradients in the different domain configurations. In addition, the deformation

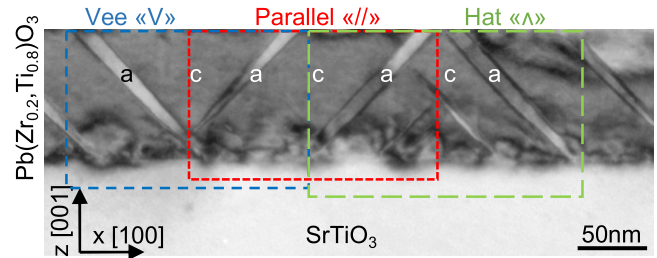


**Figure 1.** TEM image of a 100 nm thick commercial  $\text{Pb}(\text{Zr}_{0.2}\text{Ti}_{0.8})\text{O}_3$  (PZT) layer epitaxially grown on a  $\text{SrTiO}_3$  (STO) substrate, containing large  $c$ -domains ( $c$ -axis and polarization along the  $[001]$  direction, vertical in the image) and needle-shaped  $a$ -domains or  $90^\circ$  domains ( $c$ -axis and polarization along the  $[100]$  direction, horizontal in the image). Three types of  $a/c/a$  domain configurations can be distinguished: *parallel-//*-shaped, *V*-shaped and *hat-^*-shaped.

maps are compared quantitatively with finite element method (FEM) simulations.

## 2. Experimental conditions and methods

The samples under investigation in this paper are two epitaxial layers of  $\text{Pb}(\text{Zr}_{0.2}\text{Ti}_{0.8})\text{O}_3$  (PZT), commercial and lab-grown. The commercial sample is a 100 nm thick layer epitaxially grown on a  $(001)$ -oriented Nb-doped  $\text{SrTiO}_3$  substrate. The lab-grown sample is a 140 nm thick layer with a 10 nm thick  $\text{SrRuO}_3$  bottom electrode grown by pulsed layer deposition (PLD) on a  $\text{TiO}_2$ -terminated  $(001)$ -oriented  $\text{SrTiO}_3$  substrate [21]. PLD was performed with a 248 nm KrF excimer laser (Lambda Physik COMPex Pro 205) and controlled *in situ* by reflection high-energy electron diffraction (RHEED) experiment. Prior to the growth, the PLD chamber was pumped down to a background pressure of  $10^{-8}$  mbar. The laser fluence, the frequency, the substrate temperature, the oxygen pressure, were  $2 \text{ J cm}^{-2}$ , 1 Hz,  $580^\circ\text{C}$  ( $600^\circ\text{C}$  for the bottom electrode) and 0.13 mbar respectively. After the growth, the films were cooled down in an oxygen pressure of 100 mbar and with a rate of  $3^\circ\text{C min}^{-1}$ . Both the commercial and the lab-grown samples were found to contain  $90^\circ$  domains as well as the three domain configurations (*parallel-//*-shaped, *V*-shaped and *hat-^*-shaped).

Cross-section thin foils were prepared using a focused ion beam (FIB) FEI Quanta 3D platform. Parallel-sided lamellae with a thickness of 100–150 nm were produced with a final milling at 5 kV.

The transmission electron microscopy images were obtained using two different microscopes. The first one is a FEI Tecnai microscope equipped with a Schottky field emission gun operated at 200 kV, an image corrector (CEOS), a single biprism and a  $2\text{k} \times 2\text{k}$  CCD camera. The second microscope is a Hitachi HF-3300 (I2TEM) equipped with a cold field emission gun operated at 300 kV, two goniometer stages (the standard stage within the pole piece gap of the objective lens and an ‘upper stage’ placed above the objective lens for Lorentz mode i.e. field-free imaging), an image corrector (CEOS B-COR), four electron biprisms (one pre-specimen and three post-specimen) and a  $4\text{k} \times 4\text{k}$  camera (OneView<sup>TM</sup> Gatan).

HRTEM was carried out using the FEI Tecnai microscope. The sample was oriented on the [010] zone-axis and the acquisition was performed at a sufficiently low magnification to image the whole film and a part of the substrate (used as a reference for the measurement of the deformation using GPA). DFEH was carried out using the Hitachi HF-3300 microscope. The sample was inserted in the upper stage in order to obtain a large holographic field-of-view. The sample was oriented a few degrees away from the zone-axis in order to increase the intensity of the diffracted beam (two-beam condition) and the incident beam was tilted to bring the chosen diffracted beam on the optical axis. The diffracted beam was then selected with an objective aperture. For each region investigated, two distinct dark-field holograms were acquired using the (002) and (200) diffracted beams. A double biprism setup, with the first biprism in a conjugate image plane to the sample and the second biprism in the shadow of the first biprism, was used to avoid Fresnel fringes [22]. The fringe spacing was 2 nm and the hologram width was 300 nm.

The high resolution images and dark-field holograms were processed using respectively, the GPA and Holodark plug-in softwares (HREM Research Inc.) for Digital Micrograph (Gatan). Phase images were reconstructed using a half-cosine mask in Fourier space. The size of the masks was chosen to achieve a spatial resolution of 2 nm for the HRTEM images and 6 nm for the dark-field holograms. Phase images reconstructed from the (002) and (200) dark-field electron holograms were aligned to calculate the 2D deformation field. The phase images were corrected for large scale distortions introduced by the projector lenses of the microscope and the camera distortions [23]. After calculation of the deformation maps, an additional Gaussian spatial averaging of 2 nm was applied to reduce the noise. In the following sections, one example of deformation field is given for each of the three domain configurations. Qualitatively, those fields were found to be similar for the two samples investigated.

Finite element method simulations based on the anisotropic elastic theory were performed in 2D using the structural mechanics module of COMSOL Multiphysics. We assumed that the residual strain distribution in the films is mainly due to geometric and mismatch constraints (*a/c* tetragonality of the material, crystal tilt between the domains, accommodation of the domain pattern on a flat substrate). Electromechanical interactions were not taken into account. The principle of the simulation is based on the attribution of initial anisotropic deformation coefficients to each domain, leading to the expansion or the contraction of the domain (similarly to a thermal expansion problem). The deformation field is then determined using the anisotropic elastic coefficients and some boundary conditions. The geometry of each *a/c/a* domain configuration (i.e. the position of the domain walls) was modeled according to the TEM images. The initial deformation coefficients were defined using the average lattice parameters of the layers and the substrate, which were measured from diffraction patterns. The elastic coefficients of the layer, were interpolated from the coefficients of  $\text{PbTiO}_3$  and  $\text{PbZrO}_3$  found in the literature [24,

25]. Concerning the boundary conditions, the bottom interface was fixed in the vertical *z* direction, so that the bottom part of the layer is constrained to be flat. The layer was not clamped in the (*x*, *y*) directions of the interface to permit the lateral relaxation. The surface of the layer was free to relax in all three directions.

### 3. Results

#### 3.1. Deformation fields in a 90° domain (*a*-domain)

Figure 2(a) shows a HRTEM image of the commercial sample, which contains a 90° domain (*a*-domain). Figure 2(b) is a magnification of the region defined by the dotted rectangle. The *a*-domain has a width of 9 nm (measured perpendicularly to the domain walls). Figures 2(c)–(f) show the deformation field obtained by GPA. The deformations are defined as:

$$\begin{aligned}\varepsilon_{zz} &= \frac{\partial u_z}{\partial z} \\ \varepsilon_{xx} &= \frac{\partial u_x}{\partial x} \\ \varepsilon_{xz} &= \frac{1}{2} \left( \frac{\partial u_z}{\partial x} + \frac{\partial u_x}{\partial z} \right) \\ R_{xz} &= \frac{1}{2} \left( \frac{\partial u_z}{\partial x} - \frac{\partial u_x}{\partial z} \right)\end{aligned}\quad (1)$$

with  $u_z$  being the displacement of the lattice planes in the out-of-plane (vertical) direction,  $u_x$  the in-plane (horizontal) displacement,  $\varepsilon_{zz}$  the out-of-plane deformation,  $\varepsilon_{xx}$  the in-plane deformation,  $\varepsilon_{xz}$  the global shear deformation and  $R_{xz}$  the rigid-body rotation (anti-clockwise positive) [17]. All three deformations and the rotation are defined using the STO substrate lattice as a reference. The normal deformations ( $\varepsilon_{zz}$  and  $\varepsilon_{xx}$ ) can alternatively be expressed as  $\varepsilon = (d_{\text{PZT}} - d_{\text{STO}})/d_{\text{STO}}$  with  $d_{\text{PZT}}$  and  $d_{\text{STO}}$  being the interplanar distances in PZT and STO respectively. Figure 3 gives the profiles extracted from these maps perpendicularly to the domain walls (along the arrows).

The average out-of-plane deformation  $\varepsilon_{zz}$  is 5.8% ( $\pm 0.5\%$ ) in the *c*-domains and 1.1% in the *a*-domain. The values are inverted for the in-plane deformation  $\varepsilon_{xx}$ . At the 90° domain wall, the strain variation is abrupt, giving a clear separation between the *a*- and the *c*-domains. This is in agreement with previous observations showing that the width of the 90° domain wall is limited to about one unit cell [26]. At the domain wall, the polarization vectors should follow a head-to-tail arrangement to minimize the bound charges [26]. The expected lattice parameters are  $a = 0.394$  nm,  $c = 0.414$  nm for the PZT [27] and  $a = 0.3905$  nm for the STO [28]. These values give mismatches of 0.9% for the *a* parameter and 6.0% for the *c* parameter of PZT, which are close to the measured deformations.

There is no significant shear deformation  $\varepsilon_{xz}$  in the image. The rotation  $R_{xz}$  relative to the substrate is 2.6° ( $\pm 0.2^\circ$ ) in the *a*-domain and  $-0.3^\circ$  in the *c*-domains, which gives a rotation of 2.9° across the domain wall. This rotation, noted  $\alpha$  in the illustration of the structure (figure 2(g)), is related to the *a/c*

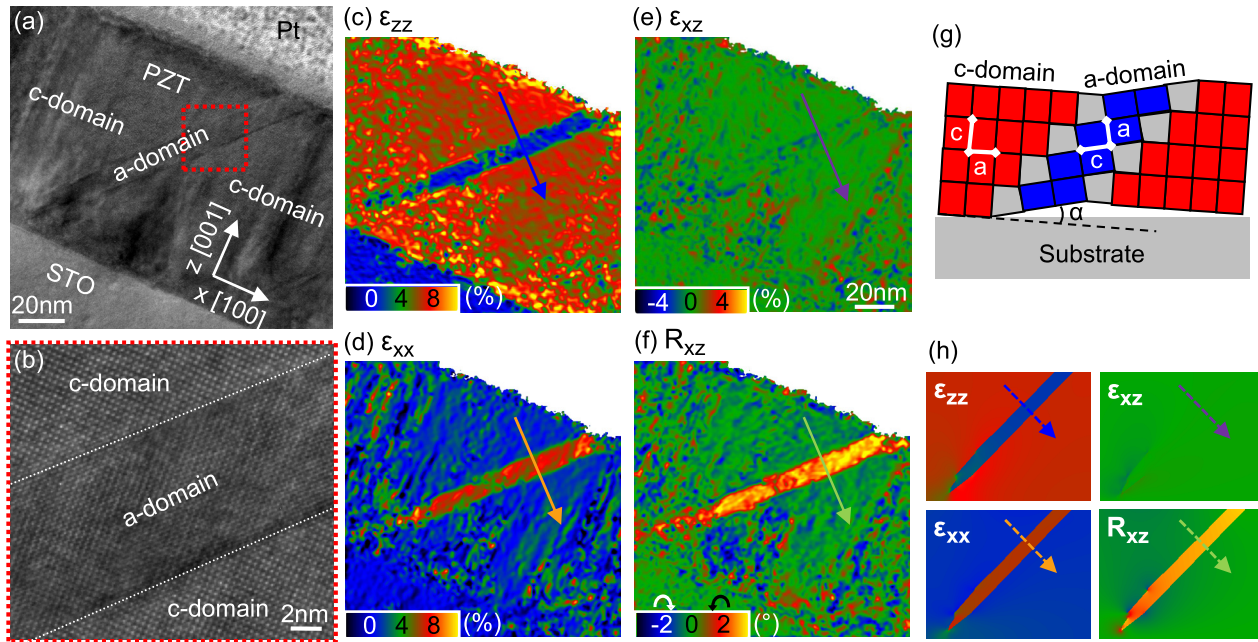


**Figure 2.** (a) HRTEM image of a needle-shaped *a*-domain in the 100 nm thick commercial PZT layer. (b) Magnified view of the *a*-domain in the region defined in (a) by a dotted rectangle. (c-f)  $\epsilon_{zz}$  out-of-plane deformation,  $\epsilon_{xx}$  in-plane deformation,  $\epsilon_{xz}$  shear deformation and  $R_{xz}$  rigid-body rotation (anti-clockwise positive) maps obtained by GPA. (g) Illustration of the lattice structure in the *c* and *a*-domains. (h) Deformation fields obtained by FEM simulations.

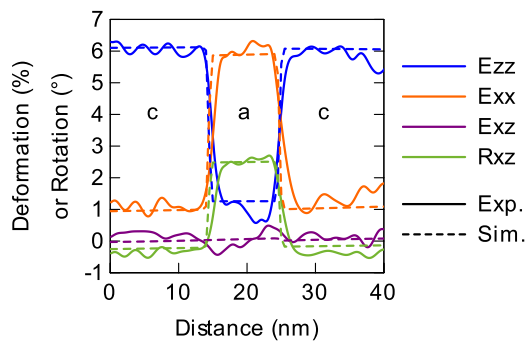


**Figure 3.** Experimental (solid lines) and simulated (dotted lines) deformation profiles extracted from the maps in figure 2 according to the arrows, across the *a*-domain. Profiles were averaged over 10 nm in the direction parallel to the domain walls.

ratio (tetragonality) according to  $\alpha = 90^\circ - 2 \arctan(a/c)$ . Using the expected lattice parameters, this expression gives  $\alpha = 2.8^\circ$ , in good agreement with the measured value.

Figure 2(h) and the dotted lines in figure 3 show the deformation maps and profiles obtained by finite element modeling. All the three simulated deformations and the rotation maps agree well with the experiment, which supports the validity of our simulation method. The simulations indicate that strain variations are likely to occur around the bottom apex of the *a*-domain due to the accommodation of the tilted domains onto the substrate. Small strain gradients ( $\leq 1\%$ ) leading to local variations of the tetragonality and so the magnitude and the direction of the polarization can be expected. The sensitivity of the HRTEM-GPA analysis ( $\pm 0.5\%$ ) is sufficient to describe the abrupt strain variations at the domain walls (of about 5%), but it is not ideal to investigate these gradients

inside the domains. For this purpose, dark-field electron holography is used in the following sections.

### 3.2. Deformation field in a *c*-domain between parallel *a*-domains

Figures 4(a) and (b) shows two dark-field holograms of the commercial sample obtained with the (002) and (200) diffracted beams, which correspond to the out-of-plane (vertical) and in-plane (horizontal) directions respectively. The holograms contain parallel *a*-domains separated by parallelogram-shaped *c*-domains.

Figure 4(c) shows a sketch of the lattice structure. The lattice rotation  $\alpha$  at the domain walls should lead to a zigzag arrangement of the whole layer (figure 4(c) top). However, the epitaxial growth requires an accommodation of this structure onto the flat surface of the substrate, which induces local strain gradients. As shown schematically by arrows, the bottom acute corner of the *c*-domains must be elongated vertically while the bottom obtuse corner must be compressed [10]. The resulting structure is sketched in the bottom part of figure 4(c).

The reconstructed deformation field is shown in figures 4(d)–(f). The  $\epsilon_{zz}$  out-of-plane deformation map (figure 4(d)) shows that the deformation is lower in the bottom obtuse corner and increases towards the bottom acute corner, in agreement with the previous illustration. The top surface is free to relax and, thus, recovers its natural zigzag shape. The  $\epsilon_{zz}$  deformation is therefore larger near the surface than in the bottom obtuse corner. The profiles in figure 4(e), extracted along the arrows show that the deformation varies along the *x* direction (black solid line), from 5.2% ( $\pm 0.1\%$ ) in the bottom

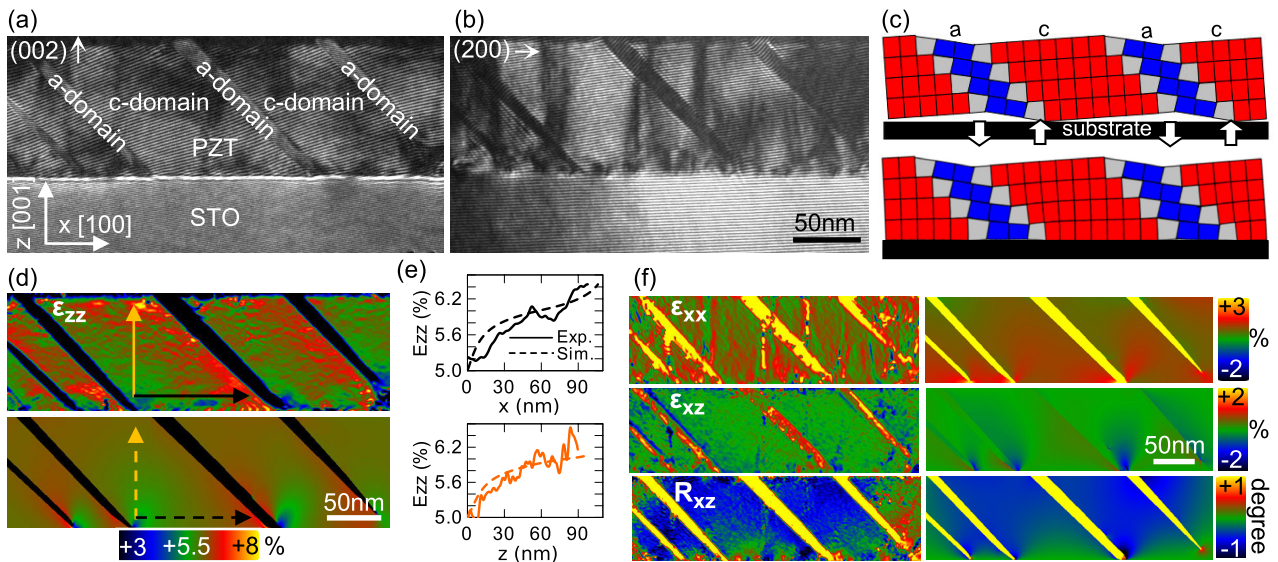


**Figure 4.** (a) (002) and (b) (200) dark-field electron holograms of the 100 nm thick commercial PZT layer, in a region containing parallel  $a$ -domains separated by parallelogram-shaped  $c$ -domains. (c) Illustration of the zigzag domain structure and the local interfacial constraints (indicated by arrows) necessary to adjust it on a flat substrate. (d) Top, experimental  $\varepsilon_{zz}$  out-of-plane deformation map; bottom,  $\varepsilon_{zz}$  map obtained by FEM simulation. (e)  $\varepsilon_{zz}$  deformation profiles extracted from (d) along the arrows in the  $c$ -domain. (f) Left, experimental  $\varepsilon_{xx}$  in-plane deformation,  $\varepsilon_{xz}$  shear deformation and  $R_{xz}$  rigid-body rotation maps. Right, corresponding deformation maps obtained by FEM simulations.

obtuse corner to 6.3% in the bottom acute corner. Along the  $z$  direction (orange solid line), it varies from 5.2% in the bottom obtuse corner to 6.2% near the surface. In other words, there are horizontal and vertical variations of about 1% over 100 nm, which correspond to gradients of  $10^5 \text{ m}^{-1}$ . The simulations (bottom image in figure 4(d) and dotted lines in figure 4(e)) are in good agreement with the experiment.

The other deformation fields (in-plane deformation  $\varepsilon_{xx}$ , shear deformation  $\varepsilon_{xz}$  and rigid-body rotation  $R_{xz}$ ) are shown in figure 4(f). The in-plane deformation map contains vertical lines where the deformation appears to vary abruptly. These are related to vertical dark lines in the (200) hologram (figure 4(b)) and most probably correspond to threading dislocations [16], due to the mismatch between STO and PZT at the growth temperature. They run from the surface of the film to the substrate interface where they are usually connected to a misfit dislocation segment [16].

The experimental shear deformation map shows some unexpected high variations in the  $a$ -domains and at the domain walls. These are artifacts due to the low contrast of the (200) hologram fringes in the  $a$ -domains. Experimentally, it is difficult to obtain a good diffraction contrast for both the  $c$ - and  $a$ -domains due to the crystal tilt between these twin domains. The rotation map shows vertical gradients in the  $c$ -domains. The rotation is nearly zero in the lower part of the  $c$ -domains because the lattice is aligned with the substrate. The rotation increases progressively (in absolute terms) along the growth direction to reach  $-0.5^\circ (\pm 0.1^\circ)$  near the top surface where the layer is free to rotate, relaxing into the zigzag shape.

In conclusion, this *parallel-//shaped* configuration contains both vertical and horizontal gradients of out-of-plane deformation. Such gradients have been observed previously in layers of  $\text{PbTiO}_3$  grown on  $\text{DyScO}_3$  substrates [10]. It has been shown that the horizontal  $\varepsilon_{zz}$  deformation gradient

(perpendicular to the polarization) induces a rotation of the polarization by the flexoelectric effect [10]. The vertical gradient of  $\varepsilon_{zz}$  (parallel to the polarization) can also modify the magnitude of the polarization by longitudinal flexoelectricity [29]. The deformation gradients measured here are significantly smaller than the gradient of  $8 \times 10^5 \text{ m}^{-1}$  reported in [10], but the conditions were completely different (larger tetragonality of  $\text{PbTiO}_3$  compared to PZT, thinner film, better match between the layer and the  $\text{DyScO}_3$  substrate, no dislocations and shorter distance between the  $a$ -domains).

### 3.3. Deformation field in a $c$ -domain between perpendicular $a$ -domains

**3.3.1. V-shaped configuration.** Figures 5(a) and (b) shows (002) and (200) dark-field electron holograms of the lab-grown sample, which contain two  $a$ -domains with opposite inclination and forming a ‘V’. The central  $c$ -domain is approximately an isosceles triangle with the base located at the top surface. The sketch in figure 5(c) illustrates the local deformations necessary to bond the domain structure onto the flat surface of the substrate. There is a vertical compression of the bottom region of the central  $c$ -domain while the  $c$ -domains at the sides are stretched. As a result of this three-point stress system, the central  $c$ -domain is bent symmetrically with respect to the mid-vertical axis and its surface takes a convex shape. This can be described as a disclination strain [6, 30].

Figure 5(d) compares the experimental and simulated deformation maps. The in-plane  $\varepsilon_{xx}$  deformation map and the profile in figure 5(f) (solid line), extracted along the blue arrow, show that the middle  $c$ -domain contains a vertical gradient of in-plane deformation. The deformation increases progressively from 1.1% ( $\pm 0.1\%$ ) at the bottom apex of the  $a$ -domains to a maximum of 1.6% near the surface. In other

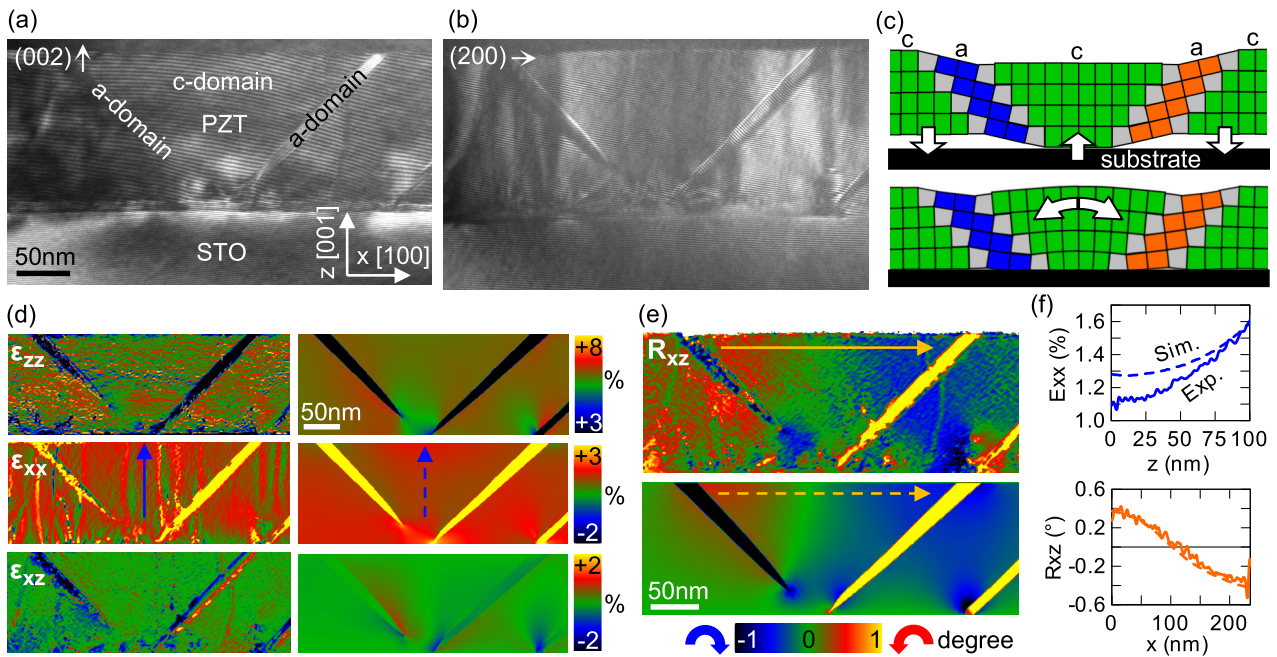


**Figure 5.** (a) (002) and (b) (200) dark-field electron holograms of the 140 nm thick lab-grown PZT layer, in a region containing two *a*-domains forming a ‘V’. (c) Illustration of the domain structure and the local interfacial constraints (indicated by arrows) necessary to adjust it on a flat substrate. (d) Left, experimental  $\varepsilon_{zz}$  out-of-plane deformation,  $\varepsilon_{xx}$  in-plane deformation and  $\varepsilon_{xz}$  shear deformation maps. Right, corresponding deformation maps obtained by FEM simulation. (e) Experimental and simulated  $R_{xz}$  rigid-body rotation maps (top and bottom respectively). (f)  $\varepsilon_{xx}$  and  $R_{xz}$  profiles extracted from ((d), (e)) along the arrows.

words: the horizontal stretching of the central *c*-domain increases as the domain walls become further apart. The deformation gradient is 0.5% over 80 nm, which corresponds to  $6 \times 10^4 \text{ m}^{-1}$ .

In the out-of-plane  $\varepsilon_{zz}$  deformation map, no significant gradient could be detected across the central *c*-domain. Only some local variations can be observed in the bottom region. The shear  $\varepsilon_{xz}$  deformation is also homogeneous in the *c*-domain. The variations observed in the *a*-domains and at the domain walls are artifacts caused by the low fringe contrast and a slight defocus of the holograms.

The rigid-body rotation map in figure 5(e) shows a rotation gradient between the two top corners of the central *c*-domain. The rotation is anti-clockwise in the top-left corner, clockwise in the top-right corner and symmetric with respect to the mid-vertical axis. The rotation profile (plain line) in figure 5(f), extracted from the map along the horizontal orange arrow, indicates that the rotation varies almost linearly between  $+0.4^\circ$  to  $-0.4^\circ$  ( $\pm 0.1^\circ$ ). The simulated deformation and rotation profiles (dotted lines) are in good agreement with the experimental ones.

In conclusion, this situation is similar to a three-point bending test where the in-plane deformation is tensile in the convex region, at the outside of the bend, and compressive in the concave region. Three-point bending is a conventional technique to introduce a transverse strain gradient in a material and investigate the associated flexoelectric response [31, 32]. The  $\varepsilon_{xx}$  deformation gradient being along the growth direction, parallel to the polarization, it should modulate only the magnitude of the polarization, without changing its direction.

**3.3.2. Hat- $\wedge$ -shaped configuration.** The holograms in figures 6(a) and (b), obtained in the lab-grown sample, show the opposite configuration of the previous one: the *a*-domains form a hat ‘ $\wedge$ ’ shape and the central *c*-domain forms an isosceles triangle with the base located at the interface. Partial *a*-domains terminating inside the layer are also present in the central *c*-domain. If we consider only the two main *a*-domains (illustration in figure 6(c)), the bottom region of the central *c*-domain is expected to be elongated vertically and the *c*-domains on the sides to be compressed. Again, this leads to a three-point stress system but with opposite stresses compared to the *V-shaped* configuration. Near the surface, the central *c*-domain should be compressed horizontally, where the two *a*-domains are the closest. Bending deformations symmetric to the mid-vertical axis are also expected. In this case, the convex side of the bend should be located near the interface with the substrate.

Experimental and simulated deformation maps are shown in figure 6(d). Simulations carried out without partial *a*-domains are also reported in order to understand the influence of the different domains on the deformation field. The  $\varepsilon_{xx}$  map and the blue profile in figure 6(e), extracted along the blue arrow, indicate a decrease of the in-plane deformation along the growth direction, from 1.9% ( $\pm 0.1\%$ ) at the bottom of the central *c*-domain to 1.1% at the top region. In other words, the horizontal compression of the central *c*-domain increases when the two main *a*-domains become closer. The simulations with and without partial *a*-domains confirm that the vertical gradient of  $\varepsilon_{xx}$  deformation is induced by the two main *a*-domains and the partial *a*-domains can slightly modify this gradient.

The  $\varepsilon_{zz}$  map and the green profile (figures 6(d) and (e)) show that the out-of-plane deformation is strong at the bottom

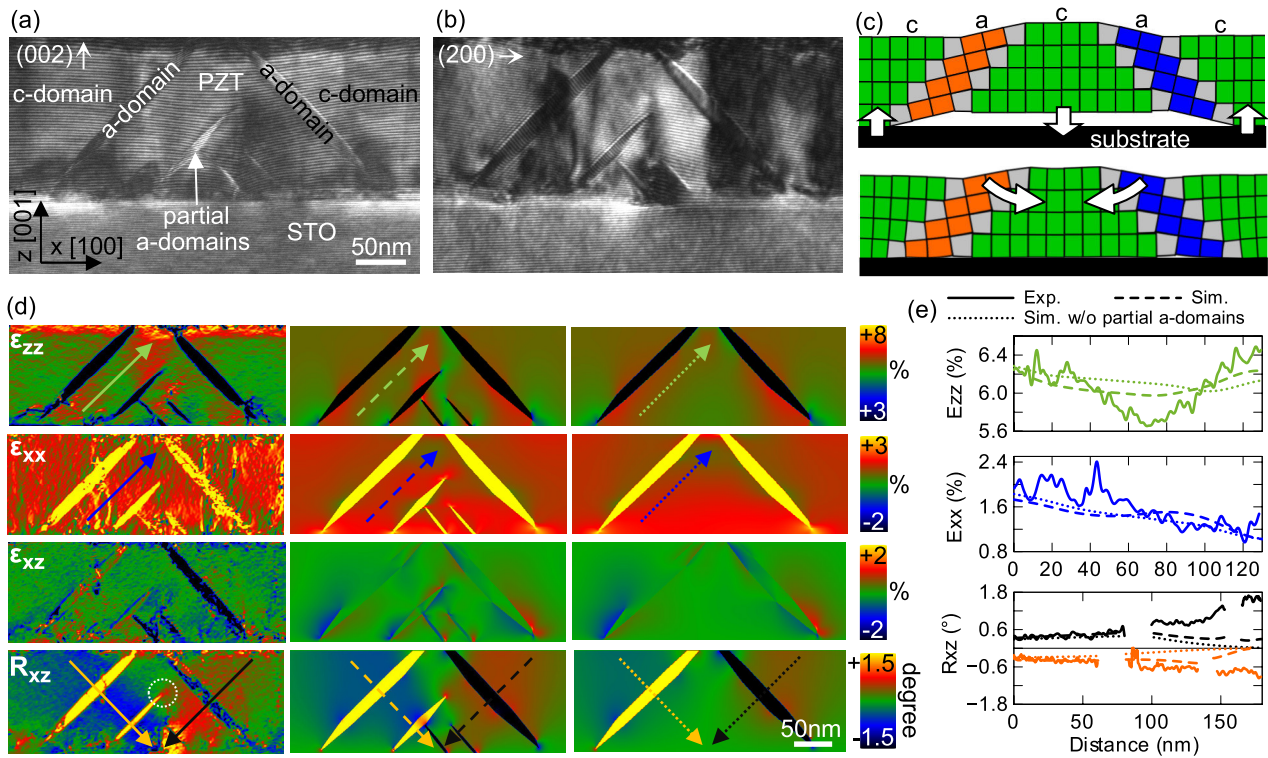


**Figure 6.** (a) (002) and (b) (200) dark-field electron holograms of the 140 nm thick lab-grown PZT layer, in a region containing two *a*-domains forming a hat ‘^’ and with partial *a*-domains in-between. (c) Illustration of the domain structure and the local interfacial constraints (indicated by arrows) necessary to adjust it on a flat substrate. (d) Left, experimental  $\epsilon_{zz}$  out-of-plane deformation,  $\epsilon_{xx}$  in-plane deformation,  $\epsilon_{xz}$  shear deformation and  $R_{xz}$  rigid-body rotation maps. Middle, corresponding deformation maps obtained by FEM simulations. Right, simulated deformation maps without partial *a*-domains. (e)  $\epsilon_{zz}$ ,  $\epsilon_{xx}$  and  $R_{xz}$  profiles extracted from (d) along the arrows. For clarity, the rotation  $R_{xz}$  in the *a*-domains is not plotted.

corners and at the top region of the central *c*-domain. The increase of  $\epsilon_{zz}$  at the bottom acute corners was previously observed and explained in the *parallel* configuration, with the difference that here both corners are acute. The simulation without partial *a*-domains shows that  $\epsilon_{zz}$  should be minimum in the middle region, at equal distance of the two bottom corners. The increase of  $\epsilon_{zz}$  in the top region can be the consequence of the horizontal compression (Poisson effect). The variations in the simulated  $\epsilon_{zz}$  map are smaller than the measured ones but qualitatively the trend is the same. The comparison of the two simulations show that the increase of the deformation in the top region is also due to the partial *a*-domains.

The rotation  $R_{xz}$  map shows two gradients: negative (clockwise) on the left-hand side and positive (anti-clockwise) on the right-hand side. The rotation field is guided by the partial *a*-domains and increases from the surface to the bottom interface. The black and orange rotation profiles in figure 6(e) extracted from the map, indicate that the rotation varies from  $0.4^\circ (\pm 0.1^\circ)$ , near the surface, to  $1.0\text{--}1.5^\circ$  near the interface. The profiles are not perfectly symmetric, which is due to the distribution of the partial *a*-domains. The simulated rotation field agrees with the experiment at the top of the layer, but the agreement is less good near the interface. Close to the interface, defects and smaller partial *a*-domains, not taken into account in the simulation, might influence the deformation field.

It is interesting to note that, at the top end of a partial *a*-domain, indicated by a white dotted circle, there is an

anticlockwise rotation field diffusing from the apex. This is in agreement with previous measurements of deformation [13] and polarization [33]. The sign of the rotation at the apex is the same as the rotation gradient around the black arrow and the two rotation fields merge together. This observation is also well reproduced in the simulated map. The agreement between the rotation at the apex of the partial *a*-domain and the surrounding rotation field might help to stabilize this particular region.

In conclusion, this *hat-^*-shaped configuration contains a decreasing gradient of in-plane deformation along the growth direction, which should modulate the magnitude of the polarization in the opposite way of the *V-shaped* configuration. The direction of the polarization should not change along the axis of symmetry of the central *c*-domains, but rotations of the polarization could occur at the bottom corners due to the horizontal variations of the out-of-plane deformation.

In addition, this configuration contains some partial *a*-domains. They can be explained by both the presence of misfit dislocations, which trigger their growth, and the presence of larger perpendicular *a*-domains, which limit their extension. Partial *a*-domains are known to be unstable and their apex is very sensitive to the mechanical environment [33].

### 3.4. Mutual arrangement of the three *a/c/a* configurations

We have investigated three *a/c/a* domains configurations where the *a*-domains are *parallel-//*-shaped, *V-shaped* and

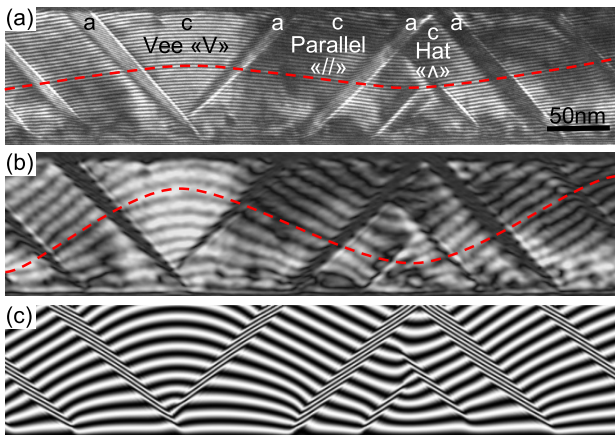


**Figure 7.** (a) (002) Dark-field hologram of the 100 nm thick commercial PZT layer in a region containing the three  $a/c/a$  configurations previously described: *V-shaped*, *parallel-//shaped* and *hat- $\Lambda$ -shaped* (from left to right). The dashed line indicates the shape of the holographic fringes in the  $c$ -domains. (Aliasing effects can give the impression that the shape of the fringes is different when looking at the image on a computer screen. Zooming in the image might be needed to avoid this artifact.) (b) Moiré image showing a magnified representation of the holographic fringes. (c) Moiré image calculated from a finite element simulation.

*hat- $\Lambda$ -shaped*. After describing independently each configuration, we can study how they combine together. Figure 7(a) shows a (002) hologram of the commercial PZT layer, which contains those three domain configurations. In order to magnify the fringes further (i.e. reduce the periodicity) and amplify their curvature, the hologram was superimposed with a fringe pattern of constant spacing. Figure 7(b) shows the amplitude image of the resulting moiré pattern. The curvature of the fringes indicates a wavy arrangement of the lattice planes where the up and down waves are due to the bending deformations in the *V-shaped* and  $\Lambda$ -shaped configurations respectively. Figure 7(c) is a moiré image obtained from a FEM simulation, which shows a trend similar to the experimental result. The *parallel-//shaped* configuration provides an ideal connection between the *V* and  $\Lambda$  configurations thanks to the inclination of the planes. However, we have also observed that the ordering of the three configurations is not always the same through the film. *V* and  $\Lambda$  configurations can be next to each other or separated by a different number of *parallel* configurations, which can change the regularity of the undulations. The periodicity of the domains is related to the volume fraction of  $a$ -domains versus  $c$ -domains. A statistical analysis of the TEM images has shown that the  $a$ -domains occupy 18% of the cross-sectional area, in the commercial PZT layer, and 10% in the lab-grown sample. The domain fraction might be influenced by the presence of a  $\text{SrRuO}_3$  bottom electrode in the lab-grown sample (the commercial sample is grown on a Nb-doped  $\text{SrTiO}_3$  substrate), which might lead to slightly different electrostatic boundary conditions [34] and can play a role in the strain relaxation [35]. However, interestingly, the prevalence of three domain configurations was found to be the same for both samples: about 65% of the configurations were *parallel* and 35% were *V* or *hat* (these two are in equal proportion).

## 4. Discussion

We have described three  $a/c/a$  domain configurations that exhibit different deformation gradients induced by the clamping of the twinned patterns onto the flat surface of the substrate. The order of magnitude of the deformation gradients observed in this study is  $10^4$  to  $10^5 \text{ m}^{-1}$ . This is significantly larger than the gradients obtained on a macroscopic scale by mechanical bending of bulk samples ( $\leq 1 \text{ m}^{-1}$  [36]). Furthermore, these gradients extend over a scale of a hundred of nanometers which provides an interesting range for the design of nano-devices. For comparison, stronger strain gradients such as interfacial strain relaxation (on the order of  $10^6 \text{ m}^{-1}$ ) [37, 38] or those measured near the core of misfit dislocations ( $10^7 \text{ m}^{-1}$ ) occur on a limited scale of about ten nanometers [39, 40]. Recently, more exotic domain configurations such as flux-closure quadrants [41, 42] and polar vortices [43] have been obtained in  $\text{PbTiO}_3$  layers sandwiched between  $\text{SrTiO}_3$  layers. Those structures exhibit huge strain gradients but they require symmetric boundary conditions. In average, the different strain gradients involved in such flux-closure systems should compensate each other. So, in practice it might be complicated to take advantage of those gradients for piezo/ferroelectric applications.

Here, the strength of the strain gradients induced by the  $a/c$  twins is related to the distance between the  $a$ -domains and the rotation angle at the domain walls. Those parameters can be tuned to some extent by strain engineering i.e. by choosing the adequate substrate, the thickness of the layer and the tetragonality of the perovskite [44]. On the other hand, the regularity of the lattice waves is determined by the change of inclination of the  $a$ -domains. It is possible that dislocations, due to the mismatch between the PZT layer and the STO substrate, favor the formation of  $a$ -domains of different inclinations. Indeed, defects are known to act as nucleation sites for the  $a/c$  domain walls [45, 46] and superdomain boundaries [47]. A preferential formation of *parallel-//shaped* configurations was observed for instance in  $\text{PbTiO}_3$  and PZT layers grown on a well-matched  $\text{DyScO}_3$  substrate, which are nearly defect-free [9, 48]. On the contrary, in the films investigated here, *V-shaped* and  $\Lambda$ -shaped configurations were frequently observed. Therefore, the concentration of defects could be a controlling parameter for the formation of those different domain configurations.

Strain gradients are known to influence different functional properties of the films [29, 49]. For instance, the strain gradients induced by dislocations and vacancies can reduce the permittivity and lead to a smearing of the dielectric peak at the Curie temperature [37]. They can lead to an imprinted state characterized by an asymmetric switching behavior under electric field and shifted hysteresis loops [11–13]. Strain gradients can even switch the polarization, for example by bending the substrate [50] or by applying a local pressure with the tip of an atomic force microscope [51]. Therefore, the local ferroelectric switching behavior in the three domain configurations investigated here should exhibit different asymmetries due to the different orientation of the strain gradients. The present description of the strain should help future studies to explain

such unusual effects under application of an external electric or a stress field.

Concerning the piezoelectric properties, it has been shown that bending deformations can influence the piezo-response of PZT samples, for instance when using an elastomeric substrate to create sinusoidally deformed stripes [52, 53]. Such wavy samples are also exploited for the collection of charges induced by the direct piezoelectric effect [54]. In those wavy structures, the piezoelectric properties are enhanced in the regions where the strain gradients are maximum (at the apexes of the bends). Therefore, the nanoscale waviness of the lattice planes introduced here by the different *a/c/a* configurations might influence the local piezoelectric properties in a similar way. In addition, in the *parallel-/-shaped* configuration, a continuous rotation of the polarization is expected across the film due to the horizontal gradient of out-of-plane deformation [10]. Rotation of the polarization is a characteristic of PZT samples having a composition close to the morphotropic boundary (MPB) and those samples exhibit also large piezoelectric coefficients [55, 56]. Finally, in the *hat-^shaped* configuration, we have observed that there is a preferential formation of partial 90° domains terminating inside the films. Previously, such domains have been stabilized in composition graded PZT layers [13]. It has been shown that they can easily grow to the surface or contract to the substrate under electric field, leading to a large piezo-response in their vicinity [13]. Consequently, the deformation fields involved in special domain configurations such as this *hat* arrangement might provide an alternative route for the control of mobile ferroelastic domains.

## 5. Conclusion

We have investigated the strain state and the polydomain configuration of  $\text{Pb}(\text{Zr}_{0.2}\text{Ti}_{0.8})\text{O}_3$  thin films grown on  $\text{SrTiO}_3$  substrates using two TEM strain measurement techniques: geometrical phase analysis (GPA) method of HRTEM images and dark-field electron holography (DFEH). We have described three *a/c/a* domain configurations, which contain different deformation fields and have a different influence on the ferroelectric polarization. If the domain walls of the successive domains are parallel, the *c*-domain contains both vertical and horizontal gradients of out-of-plane deformation. The horizontal gradient should induce a rotation of the polarization and then a deviation from the vertical direction [10]. If the *a/c* domain walls are perpendicular and form a ‘V’ or a ‘^’, the *c*-domain undergoes a flexural distortion, similar to a three-point bending test, with the convex side of the bend oriented towards the surface (V) or the substrate (^). The *c*-domain contains a vertical gradient of in-plane deformation (transverse gradient), which should modulate the magnitude of the polarization without varying its direction. The alternation of the three domain configurations leads to an undulation of the lattice planes. The deformation gradients measured here are on the order of  $10^4$ – $10^5$   $\text{m}^{-1}$  and extend over a scale of about 100 nm. The measurements are globally in good agreement with finite element simulations.

In conclusion, the relative orientation of neighboring *a/c* domain walls can have a profound influence on the local strain gradients and should lead to modifications of the dielectric, ferroelectric and piezoelectric properties.

## Acknowledgments

This work was funded through the European Metrology Research Programme (EMRP) Project IND54 Nanostrain. The EMRP is jointly funded by the EMRP participating countries within EURAMET and the European Union. The authors acknowledge the European Union under the Seventh Framework Programme under a contract for an Integrated Infrastructure Initiative Reference 312483-ESTEEM2. The authors acknowledge the ‘Conseil Regional Midi-Pyrénées’ and the European FEDER for financial support within the CPER program. This work has been supported by the French National Research Agency under the ‘Investissement d’Avenir’ program reference No. ANR-10-EQPX-38-01. TD acknowledges funding from the European Research Council (ERC) under the European Union’s Seventh Framework Programme (FP7/2007-2013)/ERC Grant Agreement No. 320832. Prof. R Dunin-Borkowski is acknowledged for reading and commenting on the manuscript. Dr. G Catalan is also thanked for discussion.

## ORCID iDs

T Denneulin  <https://orcid.org/0000-0001-7350-7943>

## References

- [1] Dawber M, Rabe K M and Scott J F 2005 Physics of thin-film ferroelectric oxides *Rev. Mod. Phys.* **77** 1083–130
- [2] Murali P 2008 Recent progress in materials issues for piezoelectric MEMS *J. Am. Ceram. Soc.* **91** 1385–96
- [3] Pompe W, Gong X, Suo Z and Speck J S 1993 Elastic energy release due to domain formation in the strained epitaxy of ferroelectric and ferroelastic films *J. Appl. Phys.* **74** 6012–9
- [4] Roitburd A L 1976 Equilibrium structure of epitaxial layers *Phys. Status Solidi* **37** 329–39
- [5] Kwak B S, Erbil A, Budai J D, Chisholm M F, Boatner L A and Wilkens B J 1994 Domain formation and strain relaxation in epitaxial ferroelectric heterostructures *Phys. Rev. B* **49** 14865–79
- [6] Pertsev N A and Zembilgotov A G 1995 Energetics and geometry of 90° domain structures in epitaxial ferroelectric and ferroelastic films *J. Appl. Phys.* **78** 6170–80
- [7] Karthik J, Damodaran A R and Martin L W 2012 Effect of 90° domain walls on the low-field permittivity of  $\text{PbZr}_{0.2}\text{Ti}_{0.8}\text{O}_3$  thin films *Phys. Rev. Lett.* **108** 167601
- [8] Zednik R J, Varatharajan A, Oliver M, Valanoor N and McIntyre P C 2011 Mobile ferroelastic domain walls in nanocrystalline PZT films: the direct piezoelectric effect *Adv. Funct. Mater.* **21** 3104–10
- [9] Vlooswijk A H G, Noheda B, Catalan G, Janssens A, Barcones B, Rijnders G, Blank D H A, Venkatesan S, Kooi B and de Hosson J T M 2007 Smallest 90° domains in epitaxial ferroelectric films *Appl. Phys. Lett.* **91** 112901
- [10] Catalan G, Lubk A, Vlooswijk A H G, Snoeck E, Magen C, Janssens A, Rispens G, Rijnders G, Blank D H A and

- Noheda B 2011 Flexoelectric rotation of polarization in ferroelectric thin films *Nat. Mater.* **10** 963–7
- [11] Lee D, Yoon A, Jang S Y, Yoon J-G, Chung J-S, Kim M, Scott J F and Noh T W 2011 Giant flexoelectric effect in ferroelectric epitaxial thin films *Phys. Rev. Lett.* **107** 057602
- [12] Tagantsev A K and Gerra G 2006 Interface-induced phenomena in polarization response of ferroelectric thin films *J. Appl. Phys.* **100** 051607
- [13] Agar J C *et al* 2016 Highly mobile ferroelastic domain walls in compositionally graded ferroelectric thin films *Nat. Mater.* **15** 549–56
- [14] Alpay S P, Nagarajan V, Bendersky L A, Vaudin M D, Aggarwal S, Ramesh R and Roytburd A L 1999 Effect of the electrode layer on the polydomain structure of epitaxial  $\text{PbZr}_{0.2}\text{Ti}_{0.8}\text{O}_3$  thin films *J. Appl. Phys.* **85** 3271–7
- [15] Ganpule C S, Nagarajan V, Li H, Ogale A S, Steinhauer D E, Aggarwal S, Williams E, Ramesh R and De Wolf P 2000 Role of  $90^\circ$  domains in lead zirconate titanate thin films *Appl. Phys. Lett.* **77** 292–4
- [16] Vrejoiu I, Rhun G L, Zakharov N D, Hesse D, Pintilie L and Alexe M 2006 Threading dislocations in epitaxial ferroelectric  $\text{PbZr}_{0.2}\text{Ti}_{0.8}\text{O}_3$  films and their effect on polarization backswitching *Phil. Mag.* **86** 4477–86
- [17] Hýtch M, Snoeck E and Kilaas R 1998 Quantitative measurement of displacement and strain fields from HREM micrographs *Ultramicroscopy* **74** 131–46
- [18] Hýtch M, Houdellier F, Hüe F and Snoeck E 2008 Nanoscale holographic interferometry for strain measurements in electronic devices *Nature* **453** 1086–9
- [19] Béché A, Rouvière J, Barnes J and Cooper D 2013 Strain measurement at the nanoscale: comparison between convergent beam electron diffraction, nano-beam electron diffraction, high resolution imaging and dark field electron holography *Ultramicroscopy* **131** 10–23
- [20] Cooper D, Denneulin T, Bernier N, Béché A and Rouvière J-L 2016 Strain mapping of semiconductor specimens with nm-scale resolution in a transmission electron microscope *Micron* **80** 145–65
- [21] Koster G, Kropman B L, Rijnders G J H M, Blank D H A and Rogalla H 1998 Quasi-ideal strontium titanate crystal surfaces through formation of strontium hydroxide *Appl. Phys. Lett.* **73** 2920–2
- [22] Harada K, Tonomura A, Togawa Y, Akashi T and Matsuda T 2004 Double-biprism electron interferometry *Appl. Phys. Lett.* **84** 3229–31
- [23] Hüe F, Johnson C L, Lartigue-Korinek S, Wang G, Buseck P R and Hýtch M J 2005 Calibration of projector lens distortions *J. Electron Microsc.* **54** 181–90
- [24] Piskunov S, Heifets E, Eglitis R I and Borstel G 2004 Bulk properties and electronic structure of  $\text{SrTiO}_3$ ,  $\text{BaTiO}_3$ ,  $\text{PbTiO}_3$  perovskites: an *ab initio* HF/DFT study *Comput. Mater. Sci.* **29** 165–78
- [25] Pandech N, Sarasamak K and Limpijumnong S 2013 Sound velocities and elastic properties of  $\text{PbTiO}_3$  and  $\text{PbZrO}_3$  under pressure: first principles study *Ceram. Int.* **39** S277–81 (*The 8th Asian Meeting on Electroceramics (AMEC-8)*)
- [26] Gao P, Britson J, Jokisaari J R, Nelson C T, Baek S-H, Wang Y, Eom C-B, Chen L-Q and Pan X 2013 Atomic-scale mechanisms of ferroelastic domain-wall-mediated ferroelectric switching *Nat. Commun.* **4** 2791
- [27] Shirane G and Suzuki K 1952 Crystal structure of  $\text{Pb}(\text{Zr-Ti})\text{O}_3$  *J. Phys. Soc. Japan* **7** 333
- [28] Madelung O, Rössler U and Schulz M (ed) 2000 *SrTiO<sub>3</sub> Crystal Structure and Lattice Parameters* (Berlin: Springer) pp 1–3
- [29] Zubko P, Catalan G and Tagantsev A K 2013 Flexoelectric effect in solids *Annu. Rev. Mater. Res.* **43** 387–421
- [30] de Wit R 1972 Partial disclinations *J. Phys. C: Solid State Phys.* **5** 529
- [31] Cross L E 2006 Flexoelectric effects: charge separation in insulating solids subjected to elastic strain gradients *J. Mater. Sci.* **41** 53–63
- [32] Zubko P, Catalan G, Buckley A, Welche P R L and Scott J F 2007 Strain-gradient-induced polarization in  $\text{SrTiO}_3$  single crystals *Phys. Rev. Lett.* **99** 167601
- [33] Gao P *et al* 2014 Ferroelastic domain switching dynamics under electrical and mechanical excitations *Nat. Commun.* **5** 3801
- [34] Li Y L, Hu S Y, Liu Z K and Chen L Q 2002 Effect of electrical boundary conditions on ferroelectric domain structures in thin films *Appl. Phys. Lett.* **81** 427–9
- [35] Shelke V, Mazumdar D, Srinivasan G and Gupta A 2011 The role of  $\text{SrRuO}_3$  bottom layer in strain relaxation of  $\text{BiFeO}_3$  thin films deposited on lattice mismatched substrates *J. Appl. Phys.* **109** 07D914
- [36] Ma W and Cross L E 2003 Strain-gradient-induced electric polarization in lead zirconate titanate ceramics *Appl. Phys. Lett.* **82** 3293–5
- [37] Catalan G, Noheda B, McAneney J, Sinnamon L J and Gregg J M 2005 Strain gradients in epitaxial ferroelectrics *Phys. Rev. B* **72** 020102
- [38] Lee D and Noh T W 2012 Giant flexoelectric effect through interfacial strain relaxation *Phil. Trans. R. Soc. Lond. A* **370** 4944–57
- [39] Nagarajan V, Jia C L, Kohlstedt H, Waser R, Misirlioglu I B, Alpay S P and Ramesh R 2005 Misfit dislocations in nanoscale ferroelectric heterostructures *Appl. Phys. Lett.* **86** 192910
- [40] Chu M-W, Szafraniak I, Scholz R, Harnagea C, Hesse D, Alexe M and Gosele U 2004 Impact of misfit dislocations on the polarization instability of epitaxial nanostructured ferroelectric perovskites *Nat. Mater.* **3** 87–90
- [41] Tang Y L *et al* 2015 Observation of a periodic array of flux-closure quadrants in strained ferroelectric  $\text{PbTiO}_3$  films *Science* **348** 547–51
- [42] Tang Y L *et al* 2017 3D polarization texture of a symmetric 4-fold flux closure domain in strained ferroelectric  $\text{PbTiO}_3$  films *J. Mater. Res.* **32** 957–67
- [43] Yadav A K *et al* 2016 Observation of polar vortices in oxide superlattices *Nature* **530** 198–201
- [44] Schlom D G, Chen L-Q, Eom C-B, Rabe K M, Streiffer S K and Triscone J-M 2007 Strain tuning of ferroelectric thin films *Annu. Rev. Mater. Res.* **37** 589–626
- [45] Su D, Meng Q, Vaz C A F, Han M-G, Segal Y, Walker F J, Sawicki M, Broadbridge C and Ahn C H 2011 Origin of  $90^\circ$  domain wall pinning in  $\text{Pb}(\text{Zr}_{0.2}\text{Ti}_{0.8})\text{O}_3$  heteroepitaxial thin films *Appl. Phys. Lett.* **99** 102902
- [46] Kiguchi T, Aoyagi K, Ehara Y, Funakubo H, Yamada T, Usami N and Konno T J 2011 Configuration and local elastic interaction of ferroelectric domains and misfit dislocation in  $\text{PbTiO}_3/\text{SrTiO}_3$  epitaxial thin films *Sci. Technol. Adv. Mater.* **12** 034413
- [47] Everhardt A S, Matzen S, Domingo N, Catalan G and Noheda B 2016 Ferroelectric domain structures in low-strain  $\text{BaTiO}_3$  *Adv. Electron. Mater.* **2** 1500214
- [48] Wei X-K, Sluka T, Fraygola B, Feigl L, Du H, Jin L, Jia C-L and Setter N 2017 Controlled charging of ferroelastic domain walls in oxide ferroelectrics *ACS Appl. Mater. Interfaces* **9** 6539–46
- [49] Nguyen T D, Mao S, Yeh Y-W, Purohit P K and McAlpine M C 2013 Nanoscale flexoelectricity *Adv. Mater.* **25** 946–74
- [50] Gruverman A, Rodriguez B J, Kingon A I, Nemanich R J, Tagantsev A K, Cross J S and Tsukada M 2003 Mechanical stress effect on imprint behavior of integrated ferroelectric capacitors *Appl. Phys. Lett.* **83** 728–30
- [51] Lu H, Bark C-W, Esque de los Ojos D, Alcalá J, Eom C B, Catalan G and Gruverman A 2012 Mechanical writing of ferroelectric polarization *Science* **336** 59–61

- [52] Qi Y, Kim J, Nguyen T D, Lisko B, Purohit P K and McAlpine M C 2011 Enhanced piezoelectricity and stretchability in energy harvesting devices fabricated from buckled PZT ribbons *Nano Lett.* **11** 1331–6
- [53] Feng X, Yang B D, Liu Y, Wang Y, Dagdeviren C, Liu Z, Carlson A, Li J, Huang Y and Rogers J A 2011 Stretchable ferroelectric nanoribbons with wavy configurations on elastomeric substrates *ACS Nano* **5** 3326–32
- [54] Chu B, Zhu W, Li N and Cross L E 2009 Flexure mode flexoelectric piezoelectric composites *J. Appl. Phys.* **106** 104109
- [55] Guo R, Cross L E, Park S-E, Noheda B, Cox D E and Shirane G 2000 Origin of the high piezoelectric response in  $\text{PbZr}_{1-x}\text{Ti}_x\text{O}_3$  *Phys. Rev. Lett.* **84** 5423–6
- [56] Bellaïche L, García A and Vanderbilt D 2000 Finite-temperature properties of  $\text{Pb}(\text{Zr}_{1-x}\text{Ti}_x)\text{O}_3$  alloys from first principles *Phys. Rev. Lett.* **84** 5427–30